On the Onset of a Steady State in Body-Centered Cubic Iron during Severe Plastic Deformation at Low Homologous Temperatures

A. VORHAUER and R. PIPPAN

Armco Iron was severely deformed by means of a high-performance, high-pressure torsion (HPT) tool at a hydrostatic pressure of 5.4 GPa at low homologous temperatures, T_m, between 0.08 and 0.40 T_m. The flow stress was estimated from the measured torque during severe plastic deformation (SPD). At all investigated deformation conditions, a saturation in the flow stress at large strains without any decline was obtained. It is shown that this occurrence of a "steady state" at low homologous temperatures is significantly influenced by the deformation parameters, whereby an increase in deformation temperature or a decrease in strain rate results in a decrease in onset strain and an increase in flow stress in both the steady state and the size and aspect ratio of the structural elements. The Zener–Hollomon parameter is used to analyze the mechanical and microstructural properties as a function of the processing parameters; this shows that the investigated range of deformation conditions is divided into two regimes. For comparable high-deformation temperatures, the occurrence of a steady state is ascribed to a process similar to geometric dynamic recrystallization (DRX). Possible reasons for the occurrence of a different behavior in the low homologous temperature regime are discussed; the size of the crystallites formed during straining by the subdivision of the initial grains is considered to play an important role.

I. INTRODUCTION

INTEREST in the methods of severe plastic deformation (SPD) has increased in recent years because these methods are serious candidates for providing nanograined or at least submicrometer-grained bulk metals and alloys in industrial dimensions.[1] This interest is reflected in the continuously growing number of research groups, special conferences, and papers that are focused on SPD or SPD-related topics.

The large hydrostatic pressures,[2,3] together with the special design of SPD tools[4–7] or certain ingenious processing method tricks, inhibit failure at high strains during low-temperature material processing. Topics such as microstructural fragmentation[8–10] at the early stages of SPD and the resulting mechanical properties[1,11–15] are well investigated for a wide range of materials and for different processing techniques and deformation conditions. The methods of SPD provide nearly unlimited strains at low homologous temperatures. Despite the numerous publications in this field of materials science, there actually exists no systematic investigation of the possibility of the formation of a steady state that would limit strain hardening and microstructural refinement at large strains.

The present article deals with the influence of the processing parameters temperature and strain rate on the flow stress obtained during SPD and the corresponding microstructures. It is related to the question of whether a steady state during the SPD of Armco Iron at low homologous temperatures is obtained and the possible mechanism that would provide such a steady state, even at low homologous temperatures.

II. EXPERIMENTAL PROCEDURES

A. Materials and Materials Processing

The material investigated in this study is Armco Iron; the chemical composition is given in Table I. An annealing for 1 hour at 873 K was performed on the rod-shaped base material, in order to remove existing deformation patterns. The resulting mean grain size was approximately 40 μm. To investigate the influence of temperature and strain rate on the possible occurrence of a steady state at larger plastic strains at cold-working conditions, samples have been deformed by means of high-pressure torsion (HPT), which provides well-defined and nearly pure torsional deformation of the billet. For additional details about the special design and the benefits of such a tool, see References 7 and 16. The strain is well defined as simple shear,[17] γ, and is calculated according to

R. PIPPAN, Senior Scientist and Vice Director of Erich Schmid Insitute of Materials Science, Austrian Academy of Sciences, Head of the Christian Doppler Laboratory of Local Deformation and Fracture, Jahnstr12, Leoben A-8700, Austria. Contact e-mail: pippan@unileoben.ac.at A. VORHAUER, Material Scientist at ESI, now HILTI, Liechtenstein.

Table I. Maximum Content of Impurities (Weight Percent) in the Armco Iron Used in the Experiment

Element	C	Si	Mn	P	S	Cr	Ni	Cu
Weight pct maximum	0.007	0.007	0.08	0.008	0.011	0.02	0.03	0.02

$$\gamma = \frac{2\pi r}{t} n \qquad [1]$$

where *r, t,* and *n* are the distance from the torsion axes, the thickness of the cylindrical sample, and the number of applied revolutions, respectively.

The HPT at elevated temperatures (warm HPT) was performed using the same tool, by placing both anvils and the sample into the inductor of an induction heating. A sketch of the tool used is depicted in Figure 1. For warm HPT, the loaded sample and both anvils of the tool were heated up to the deformation temperature several minutes prior to HPT processing, in order to achieve a uniform distribution of temperature that was permanently controlled by a pyrometer within ±5 K of the chosen temperature during deformation. The total torque Γ was measured at all deformation temperatures *in situ* by means of strain gages above the sample on one of the anvils. The gages were protected

from overheating by a cooling unit that was situated directly below them. After materials processing at elevated temperatures, the samples were immediately removed from the deformation zone and were cooled by putting them on a cold steel plate, in order to freeze the microstructure. Since the thickness of the sample is only 0.7 mm, the cooling to ambient temperature was very fast and the heating during HPT deformation is very small.

B. Microstructural Investigations

The microstructure was studied in a section perpendicular to the radial direction of the samples, as illustrated in Figure 2. All microstructural examinations were performed within a Zeiss 1525XP scanning electron microscope (SEM) equipped with a field emission gun by using backscattered electrons (BSE). Therefore, a perfectly flat and well-prepared surface is required. A suitable sample preparation for that purpose was found by mechanical grinding and polishing, followed by a combined etching-polishing procedure using Nital etchant and polishing with colloidal silica (60 nm) for 15 minutes.

Micrographs were captured by detecting BSEs. These micrographs allow an estimation of the typical microstructural morphology, because in a single-phase material, the energy and intensity of the BSE depend strongly on the orientation of the crystallites, with respect to the direction of the incident electron beam, among other things (the order number of elements and the topography). Accordingly, microstructural elements are observed, even if they are subgrains that are disorientated less than one degree. This technique, however, does not permit us to determine the crystallographic disorientation between crystallites. The quantification of BSE micrographs with respect to microstructural features is based on the reinforcement of the boundaries between the microstructural elements by hand-drawn bold lines. The quality of this procedure is good, because most of these lines are well supported by high contrast in the BSE micrograph. In those cases in which the gray level of the BSE micrographs changes more smoothly between adjacent microstructural elements, the lines may be frequently subjective, even though plausible. The resulting map of hand-drawn lines was automatically analyzed by the line-sectioning technique and gives the mean values of the size and aspect ratio of the
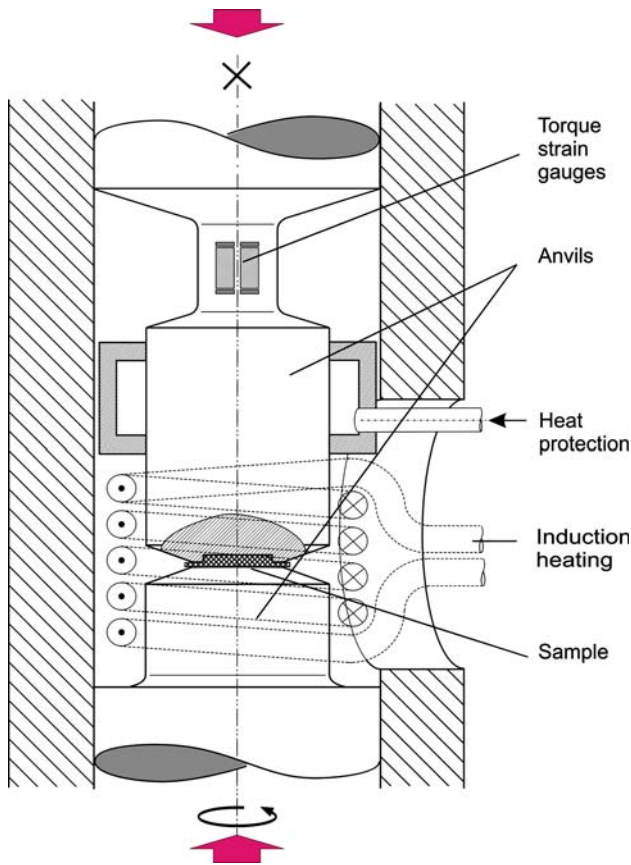

Fig. 1—Schematic representation of the HPT tool that was used, providing well-defined materials processing at low and elevated temperatures.[14]
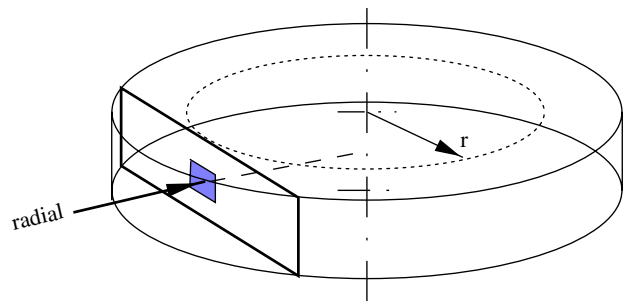

Fig. 2—Direction and position of observing microstructures.[15]

microstructural elements. This type of procedure for evaluating microstructural features was already used to analyze substructures formed during SPD.[16]

The local texture (microtexture) was measured by means of electron backscatter diffraction (EBSD), by detecting Kikuchi patterns produced by BSEs. For the present investigation, an EBSD unit from EDAX was used. The orientation maps were analyzed with respect to the disorientation between neighboring microstructural elements, resulting in boundary maps and the mean angle of disorientation between crystallites. Only EBSD scans with a very low number (below 10 pct) of misindexed pixels are used, in order to avoid significant changes of the micrographs after the cleanup procedure.

III. EXPERIMENTAL RESULTS

Samples with a diameter and height of 8 and 0.8 mm, respectively, were severely deformed at the same nominal hydrostatic pressure of $p = 5.4$ GPa, at temperatures between 77 and 723 K and strain rates $\dot{\varepsilon} = \frac{2\pi r}{t}\dot{n}$ of $2.5 \times 10^{-3} s^{-1}$ and $6.5 \times 10^{-2} s^{-1}$ at the rim of the sample ($r = 4$ mm). A summary of the results for all investigated samples, with the corresponding processing parameters, are given in Tables II and III.

A. Torque Curves

The total torque *vs* shear strain at the rim of the sample measured *in situ* during severe plastic deformations at different temperatures and at strain rates of $\dot{\varepsilon} = 2.5 \times 10^{-3} s^{-1}$ (slow) and $\dot{\varepsilon} = 6.5 \times 10^{-2} s^{-1}$ are represented in Figures 3 and 4, respectively. All curves show the same behavior: a steep rise in torque at low strains that diminishes with increasing deformation until, at a certain shear strain, γ_s, a saturation torque Γ_s, is reached. Only the curve measured at 723 K, $\dot{\varepsilon} = 2.5 \times 10^{-3} s^{-1}$, exhibits a very small smooth decrease of torque above the saturation shear strain. In all other cases, the torque above γ_s remains constant. The torque and the onset strain for saturation at different processing parameters are given in Figures 5 and 6, respectively. It is clearly seen that the processing temperature

Table III. Summary of Obtained Properties at the Onset of Steady State

| | Steady-State Properties | | | | | |
| | Torque Curve | | BSE Micrographs | | Orientation Maps, $\omega > 15$ deg | |
Sample	γ_s[1]	Γ_s (nm)	d (nm)	Aspect Ratio[1]	d (nm)	Aspect Ratio[1]
F1	24.4	195.7	127	2.67	183	2.62
F2	16.3	154.2	173	2.85	253	—
F3	10.1	121.3	244	2.90	515	2.31
F4	8.4	111.0	315	2.32	—	—
F5	6.5	104.6	369	1.73	719	2.50
S1	17.7	180.6	149	2.24	189	2.13
S2	10.0	135.3	183	2.53	—	—
S3	4.3	103.0	264	2.53	518	2.49
S4	4.7	88.0	339	2.26	—	—
S5	2.7	89.5	432	1.76	1080	2.38
C1	65.0	585.0	70	—	90	—

significantly affects both saturation torque and saturation shear strain; specifically, an increase in processing temperature causes a distinct decrease in these two parameters.

The effect of the strain rate is much smaller: an increase results in a small increase in saturation torque and onset strain.

B. Steady-State Flow Stress

The saturation flow stress is determined by the procedure described in the appendix of this work. It is reasonable to assume deformation of the material in the burr zone during HPT, because microstructural investigations have exhibited clear deformation patterns.[18] By using this assumption, it is necessary to choose a value for the parameter κ, which describes the increase in the flow stress of the materials in the burr-zone of HPT due to the higher strain rate that is present in this region. We have chosen $\kappa = 0$, because we do not know the accurate value; additionally, in the appendix it is

Table II. Summary of Processing Parameters and Dimensions of the Investigated HPT Samples (the Term *t* is the Final Thickness, and r_i and r_o are Described in the Appendix, Figure A1)

| | Deformation Conditions | | | Dimensions | | |
Sample	Temperature (K)	$\dot{\varepsilon}$ (s^{-1})	$Z = \dot{\varepsilon} \cdot \exp^{\frac{Q_{def}}{RT}}$	t (mm)	r_i (mm)	r_o (mm)
F1	293	6.55×10^{-02}	2.32×10^{53}	0.72	4.10	4.60
F2	453	6.38×10^{-02}	1.22×10^{34}	0.74	4.10	4.75
F3	543	6.53×10^{-02}	1.78×10^{28}	0.74	4.20	4.65
F4	633	6.06×10^{-02}	1.08×10^{24}	0.79	4.16	4.60
F5	723	6.45×10^{-02}	8.25×10^{20}	0.74	4.15	4.55
S1	293	2.56×10^{-03}	9.06×10^{51}	0.75	4.15	4.70
S2	453	2.56×10^{-03}	4.91×10^{32}	0.74	4.10	4.70
S3	543	2.62×10^{-03}	7.14×10^{26}	0.74	4.20	4.75
S4	633	2.52×10^{-03}	4.47×10^{22}	0.78	4.25	4.75
S5	723	2.66×10^{-03}	3.40×10^{19}	0.72	4.15	4.60
C1	77	3.42×10^{-02}	1.28×10^{206}	0.72	4.10	4.55
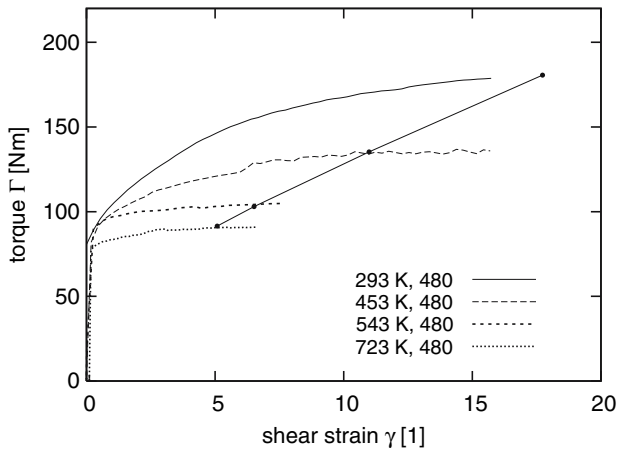
Fig. 3—*In-situ* torque curves for different temperatures at strain rate $\dot{\varepsilon} = 0.0025 \text{ s}^{-1}$.[16]
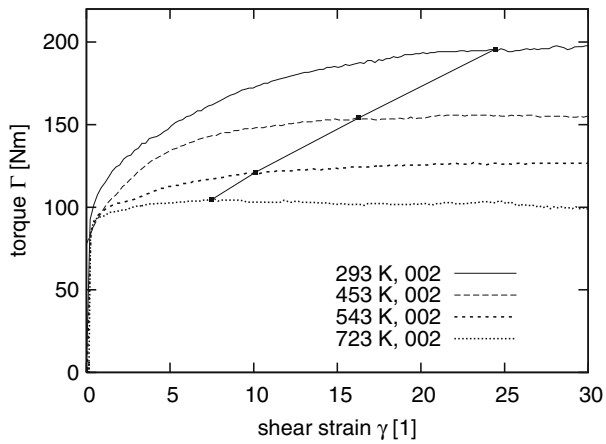

Fig. 4—*In-situ* torque curves for different temperatures at strain rate $\dot{\varepsilon} = 0.0625 \text{ s}^{-1}$.[17]
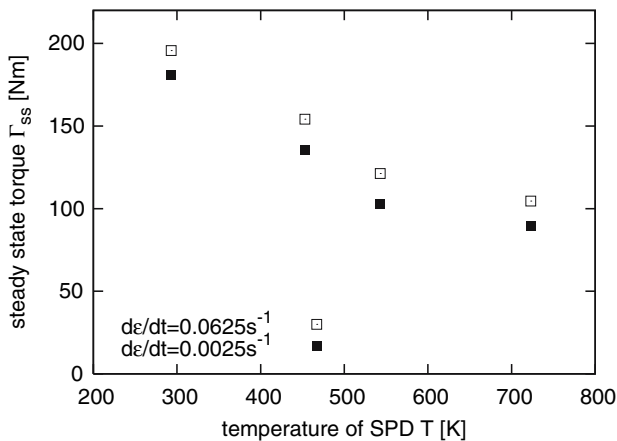

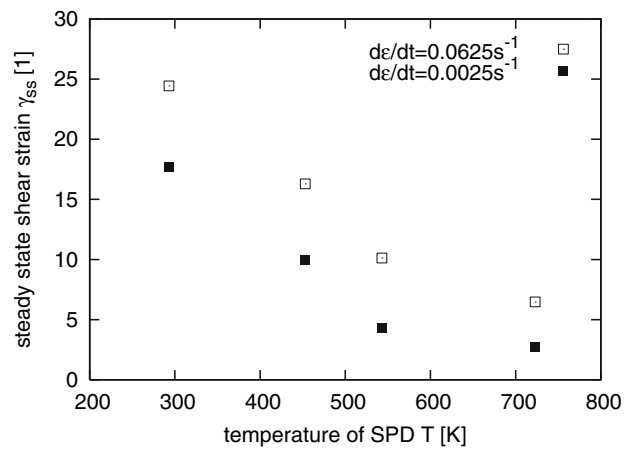Fig. 5—Steady-state torque as a function of processing temperature for both strain rates.[18]

Fig. 6—Steady-state shear strain as a function of processing temperature for both strain rates.[19]

shown that a change in this parameter does not change the resulting shear strain significantly.

C. Microstructures at the Onset of Saturation

Selected microstructures obtained at strains somewhat larger than the onset strain are depicted in Figures 7 and 8, and the evaluated characteristic parameters are shown in Figures 9 through 12.

1. Boundary maps

Boundary maps of selected deformation conditions measured in a section perpendicular to the radial direction at the onset strain of saturation are depicted in Figure 7, where boundaries that exhibit angles of disorientation of 2 through 7 deg, 7 through 15 deg, and above 15 deg are illustrated by light gray, dark gray, and black lines, respectively. From each measured boundary map, the mean size of crystallites with boundaries larger than 15 deg and their mean angle of disorientation were determined; the results are summarized in Figures 9 and 10. Approximately 400 grains are used to obtain the present result.

It is obvious that the mean size of the crystallites increases significantly with the increasing temperature of SPD. The HPT at 293 K, $2.5 \times \text{s}^{-1}$, results in crystallites that exhibit a mean size of approximately 180 nm, whereas crystallites in the range of approximately 750 nm are observed after deformation at 723 K at the same strain rate. A decrease in strain rate is comparable to an increase in deformation temperature. However, it is clearly visible that the effect of the strain rate is relatively small in relation to the effect of temperature. The mean angle of disorientation at the onset strain of saturation is in a range between 35 and 42 deg for all investigated deformation conditions, and shows a behavior opposite to that of the mean size of the crystallites: an increasing deformation temperature or decreasing strain rate results in somewhat smaller mean angles of disorientation. The difference in the mean angle of disorientation between the strain rates may be affected by the different strains at which the microstructures are taken.
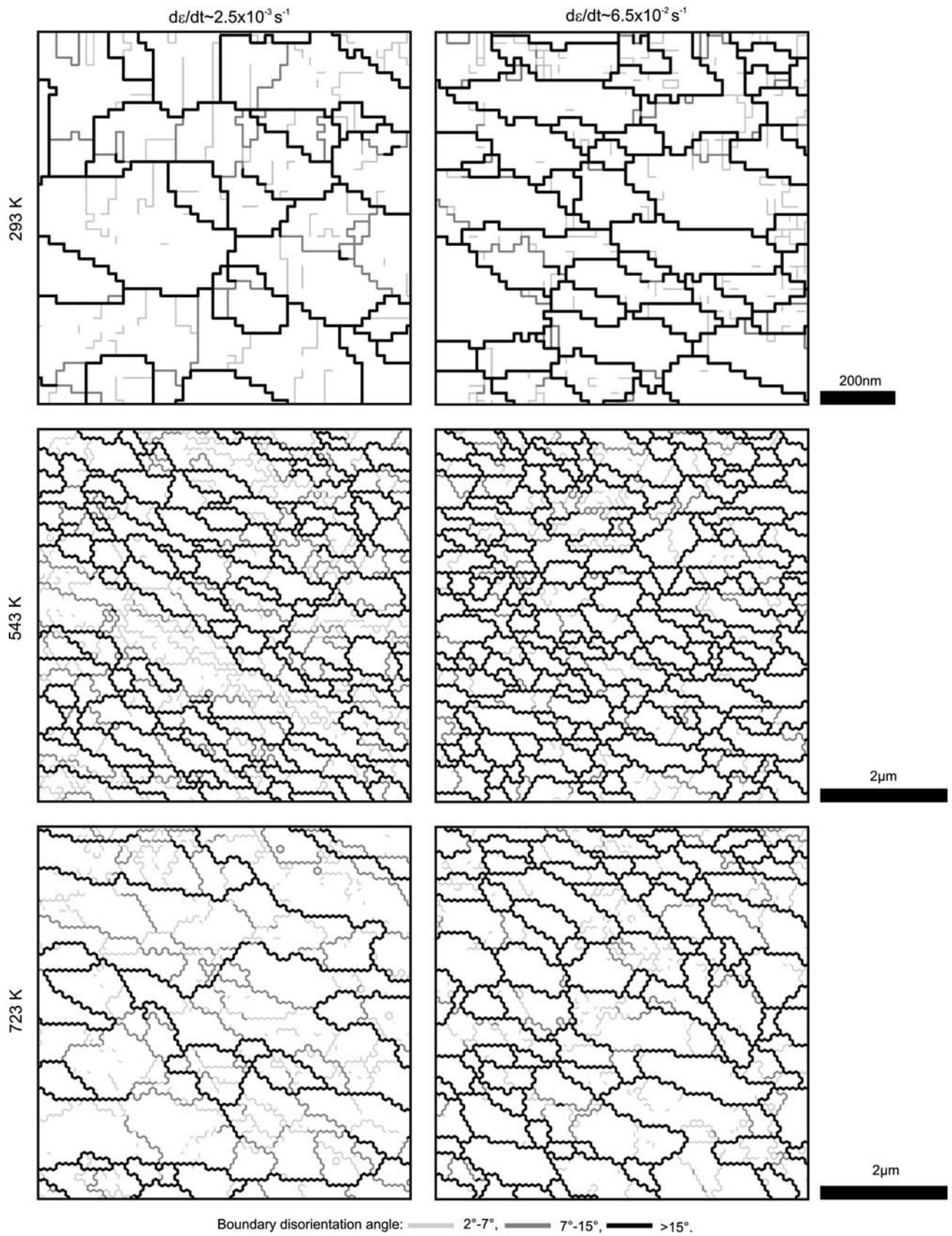
Fig. 7—Selected collection of boundary maps showing the boundary structure at strains somewhat larger than the onset strain of saturation after HPT at 293 (top row), 473, and 723 K (bottom row), at strain rates of 2.5×10^{-3} s^{-1} and 6.5×10^{-2} s^{-1} ($\gamma = 64$ at 293 K and 2.5×10^{-3} s^{-1}; $\gamma = 33$ at 293 K and 6.5×10^{-2} s^{-1}; $\gamma = 31$ at 543 K and 2.5×10^{-3} s^{-1}; $\gamma = 7$ at 543 K and 6.5×10^{-2} s^{-1}; $\gamma = 32$ at 723 K and 2.5×10^{-3} s^{-1}; and $\gamma = 6$ at 723 K and 6.5×10^{-2} s^{-1}).[20]
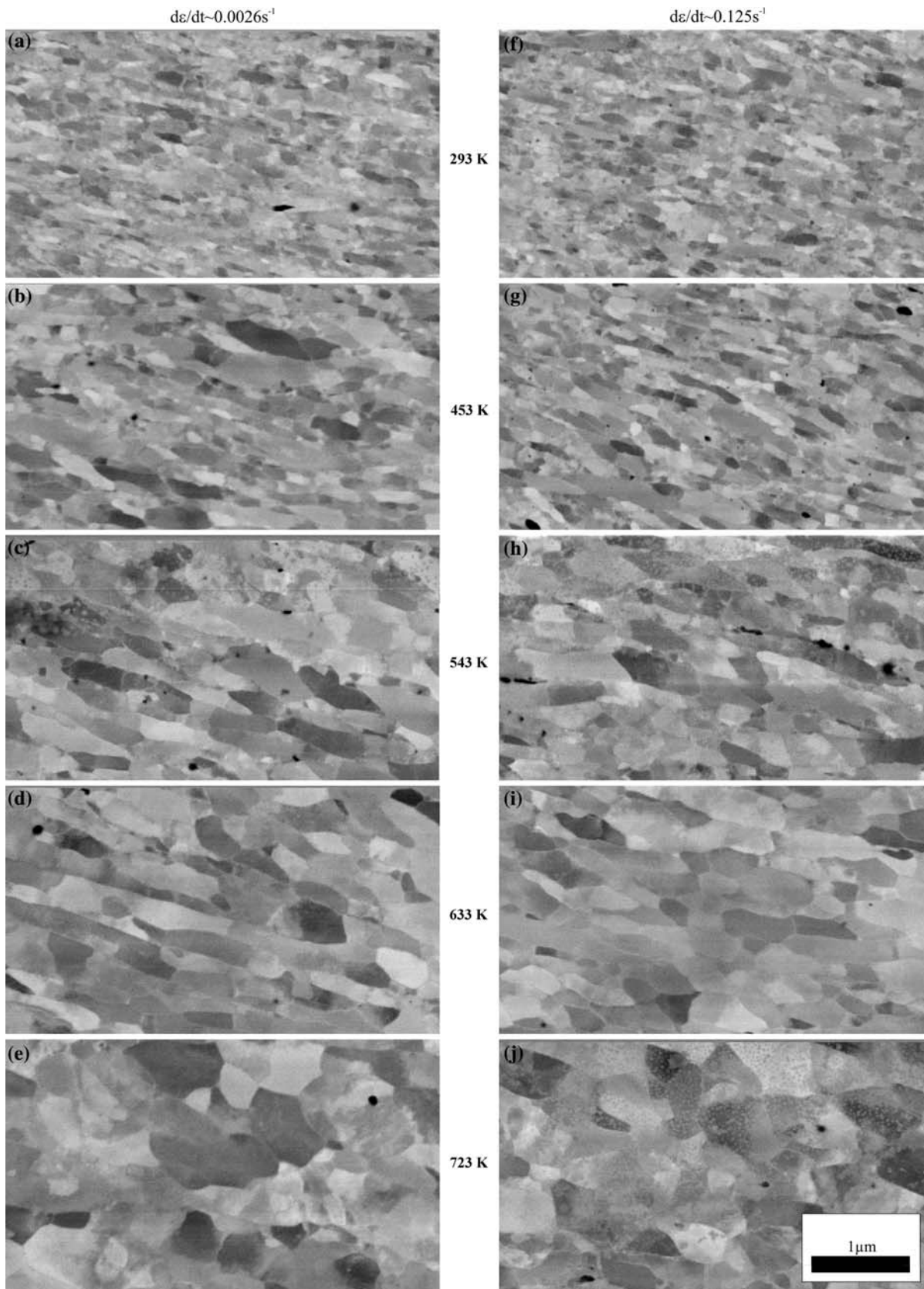
Fig. 8—Sequence of BSE micrographs in radial direction (shear direction horizontal) of the steady-state microstructure after HPT at different temperatures (rows) and strain rates (columns). The corresponding shear strains are: (*a*) 64, (*b*) 33, (*c*) 31, (*d*) 111, (*e*) 32, (*f*) 33, (*g*) 14, (*h*) 7, (*i*) 6, and (*j*) 6. All micrographs were captured at the same SEM magnification. The horizontal edge of the micrographs is parallel to the shear plane.[21]
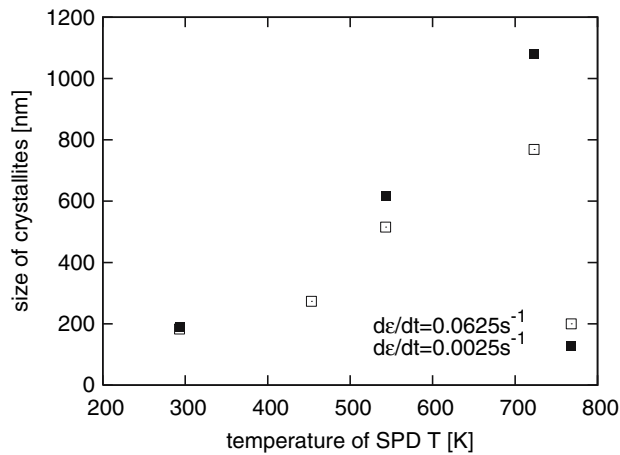
Fig. 9—Mean size of crystallites with boundary disorientation angle larger than 15 deg, obtained from orientation maps as a function of the temperature of SPD for both investigated strain rates.[22]

Fig. 10—Mean angle of disorientation of boundaries with disorientation angles larger than 15 deg obtained from orientation maps as a function of the temperature of SPD for both investigated strain rates.[22]

Fig. 11—Mean size of microstructural BSE micrographs of the steady-state microstructure.[22]
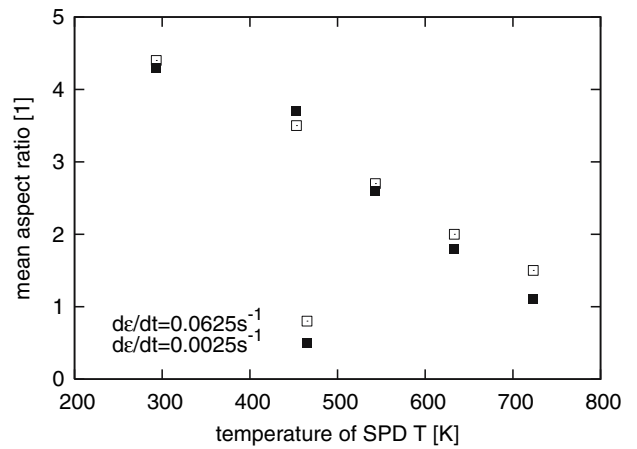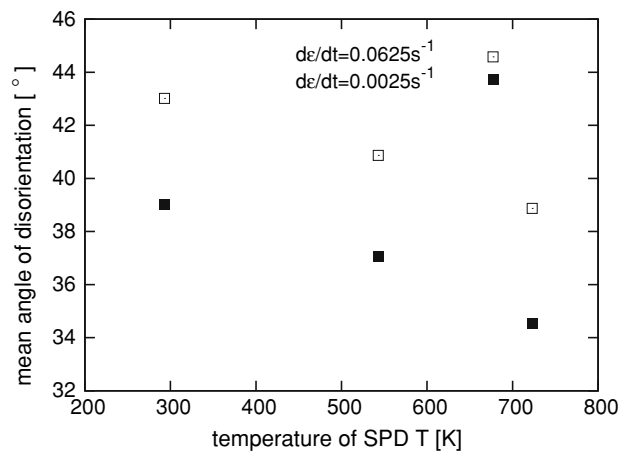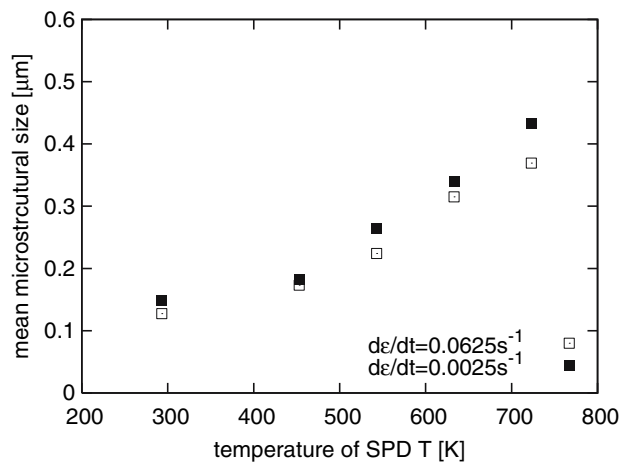

Fig. 12—Mean aspect ratio of microstructural elements for both investigated strain rates, as a function of the processing temperature determined from BSE micrographs of the steady-state microstructure.[22]

2. Substructure

Orientation maps measured by means of EBSD are of limited spatial and orientation resolution. Therefore, a sequence of BSE micrographs, all captured at the same SEM magnification in the radial direction, at a radius of 3.7 mm, shows the substructure in more detail, in Figure 8. However, it should be noted that these micrographs do not give quantitative information regarding the disorientation between adjacent microstructural elements. Instead, they provide an overview of the saturation microstructure obtained under different deformation conditions. The micrographs of the left column (Figures 8(a) through (e)) correspond to HPT deformation temperatures T of 293 (top row), 453, 543, 633, and 723 K (bottom row), respectively. The strain rate $\dot{\varepsilon}$ is $2.5 \times 10^{-3} \mathrm{s}^{-1}$, and is constant for these five samples. The most conspicuous feature of the microstructure is that the size of the microstructural elements increases from approximately 150 to 450 nm after HPT at 293 and 723 K, respectively (Figures 9 and 11). This increase in the size of the microstructural elements is in good agreement with the EBSD boundary maps. There is a large fraction of blurred boundaries after SPD at ambient temperature, which is characterized by smooth changes in grayscale between adjacent microstructural elements. With increasing processing temperature, the boundaries are more clearly visible, due to steep changes in the gray level. Additionally, it should be noted that the aspect ratio of the microstructural elements decreases with increasing temperature of SPD.

The micrographs in the right column in Figure 8 show the saturation microstructure after HPT at the same temperatures as in the left row, but at a higher strain rate, $\dot{\varepsilon}$ of $6.5 \times 10^{-2} \mathrm{s}^{-1}$. The relative changes in the size of microstructural elements, the contrast of boundaries, and the aspect ratio of the observed microstructural elements are qualitatively the same as they are for the lower strain rate. A comparison of the micrographs corresponding to the same temperature of SPD but different deformation strain rates gives the clear

impression that the microstructural elements are smaller when the materials processing is performed at higher strain rates.

These qualitative statements are supported by the quantitative results that are summarized in Figures 8 through 12, which show the mean size and the aspect ratio of the microstructural elements for the different deformation conditions.

Even if one takes into account the uncertainty in the quantification of the BSE micrographs, the main results are quite evident: the mean size of the micro-structural elements increases and their aspect ratio decreases with increasing processing temperature; the resulting microstructural sizes are smaller and their aspect ratio is somewhat larger when the strain rate is increased. It is important to note that the aspect ratio remains about the same for deformation temperatures below 543 K.

IV. DISCUSSION

In the entire range of the investigated deformation conditions, the shear stress approaches a saturation without any notable drop at large strains. When the flow stress becomes constant, the size of the structural elements, the texture, and the dislocation density also become constant. Only the disorientation distribution of the neighboring elements is somewhat changed; it becomes more and more random with increasing strain and reaches saturation at larger strains.[19] Therefore, it seems to be legitimate to term this state "steady state," consistent with the terminology used at warm- or hot-working conditions for the comparable phenomenon. The dynamic processes that provide such a steady state during SPD even at low homologous temperatures will be discussed here.

In recently published works on the structure of copper subjected to SPD,[16,20] it has been proposed that a kind of "dynamic recrystallization" (DRX) might be responsible for the occurrence of a steady state during SPD at low homologous temperatures. In the field of warm and hot working, the characteristics of DRX have been clarified.[21–25] In general, DRX is merely the terminology for numerous restoration processes, all of which result in "new" grains being developed dynamically during deformation at large strains,[26] and which include the following, among other things.

(a) Discontinuous dynamic recrystallization (DDRX), which is understood as a two-stage process composed of the nucleation and growth of recrystallized grains surrounded by high-angle boundaries (HABs); this process usually results in a significant bimodality of microstructural sizes and a distinct drop in flow stress when strain exceeds the onset strain for DRX.[27]
(b) Continuous dynamic recrystallization (CDRX),[28,29] which is considered a one-stage process, without nucleation and without any large-scale migration of HABs; terminologies such as geometric recrystallization,[30] in-situ recrystallization,[31] rotation

recrystallization,[32] extended recovery,[24,33] etc., are used for comparable mechanisms that differ in their details. The CDRX process results in a narrow distribution of microstructural sizes and the occurrence of a steady-state flow stress without any decline,[26,27,34] apart from the Taylor-factor softening[24,35] when strain exceeds the onset strain for the steady state.

The present results show clearly that the onset of a steady state during SPD in Armco Iron, and the corresponding microstructural and mechanical properties, are significantly dependent on both deformation temperature and strain rate. It is well accepted that, at temperatures at which thermally activated deformation and restoration processes occur, these two parameters of deformation are incorporated into a single (partly empirical) one, the Zener–Hollomon parameter, Z, which is defined as

$$Z = \dot{\varepsilon} \cdot \exp^{\frac{Q_{\mathrm{def}}}{RT}} \qquad [2]$$

where $\dot{\varepsilon}$ is the strain rate (s^{-1}), R is the gas constant (8.314 kJ/mol K), Q_{def} is the apparent activation energy of deformation (J/mol), and T is the absolute temperature (K). In the present study, we do not know the exact value of the activation energy of deformation, but it has been shown for many pure metals that this energy is similar to the activation energy of self diffusion.[36–39] The applied hydrostatic pressure during SPD can reduce diffusion and will consequently retard recovery kinetics. This is taken into account by using the relation between the activation energy of self diffusion Q and hydrostatic pressure p, which is given by

$$Q = Q_0 + \alpha p b^3 \qquad [3]$$

where Q_0 is the activation energy of self-diffusion at zero pressure, α is a coefficient dependent on the crystal lattice type, and b^3 is the atomic volume.[40] Taking $Q_0 = 257$ kJ/mol from Reference 41, $b = 0.248$ nm from References 41 and 42, $\alpha = 0.6$ from Reference 40, and $p = 5.4$ GPa, for α-iron, one obtains Q_{def} of about 306 kJ/mol, to estimate Z. The increase in temperature due to heat generation during deformation was neglected, because of the low strain rates and the thin samples that were deformed in this study. In Figures 13 through 16, the determined steady-state values of the size of the microstructural elements, their aspect ratio, the steady-state shear stress,* and onset

---

*Steady-state shear stress is obtained under the assumption that the material deformation was deformed during HPT in the burr zone, $\kappa = 0$. Additional details on the estimation of flow stress from torque curves measured during SPD are given in the Appendix.

---

strain are plotted against the Zener–Hollomon parameter. In addition, the number of subgrains (microstructural size taken from BSE micrographs) per grain (the size of the region bounded by HABs taken from orientation maps) as a function of Z is given in Figure 17.
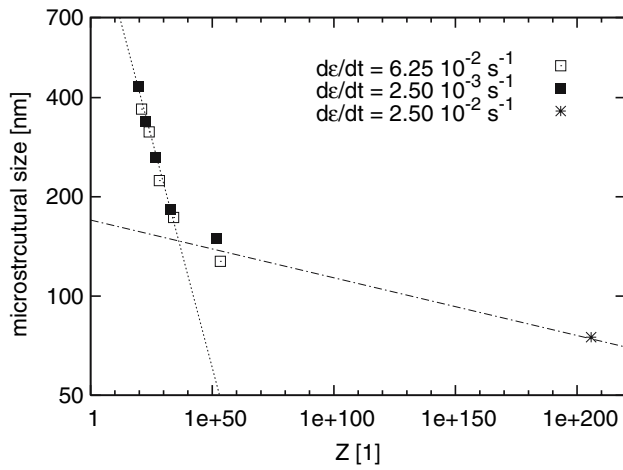
Fig. 13—Steady-state microstructural size as a function of Zener–Hollomon parameter in log (d_{ss}) vs log (Z) scale. Note the data point at very large Z obtained from a sample deformed at 77 K.[23]

Fig. 16—Steady-state shear strain as a function of Zener–Hollomon parameter in ln (γ_{ss}) vs ln (Z) scale. Note the data point at very large Z obtained from a sample deformed at 77 K.[23]

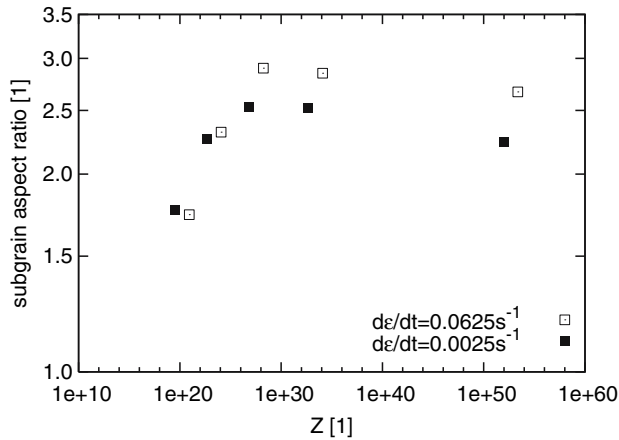Fig. 14—Steady-state aspect ratio of microstructural elements as a function of Zener–Hollomon parameter in log (b_{ss}) vs log (Z) scale.[23]
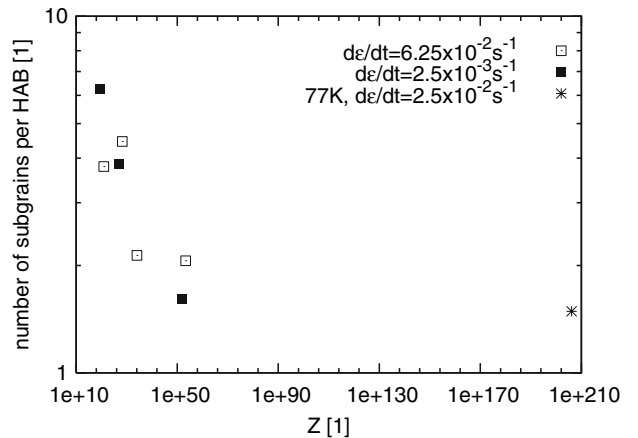
Fig. 17—Degree of fragmentation of areas bounded by HABs ($d_{HAB,EBSD}$, determined from EBSD orientation maps) into subgrains (d_{BSE}, determined from BSE micrographs) as a function of the Zener–Hollomon parameter expressed in terms of the fraction $f_{SG} = (d_{HAB,EBSD}/d_{BSE})^2$.[24]

It is evident that the steady state of each property does not gives a unique relation with rising Z. Such behavior is an indicator for a change in the underlying mechanism that is responsible for the occurrence of a steady state at given processing parameters. Thus, it is reasonable to discuss a low and a high Z regime separately.

A. Low Z Regime

In the low Z regime, no reduction of the flow stress is observed when the strain is larger than the steady-state strain; the microstructure exhibits a bimodality in microstructural sizes that is not very pronounced and that is a significant fraction of small-angle boundaries. Thus, we assume that, in the low Z regime, a process similar to geometric DRX[30,43] is responsible for the
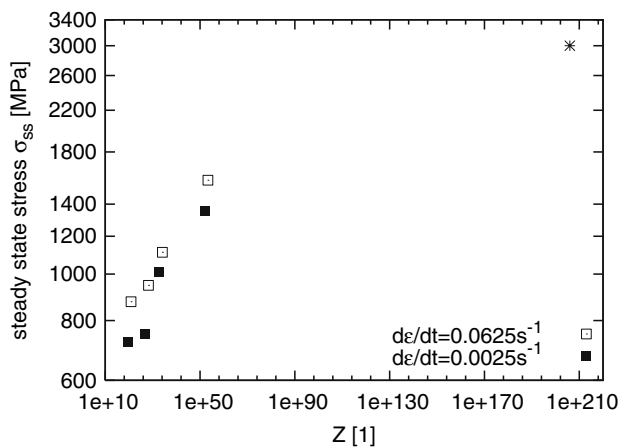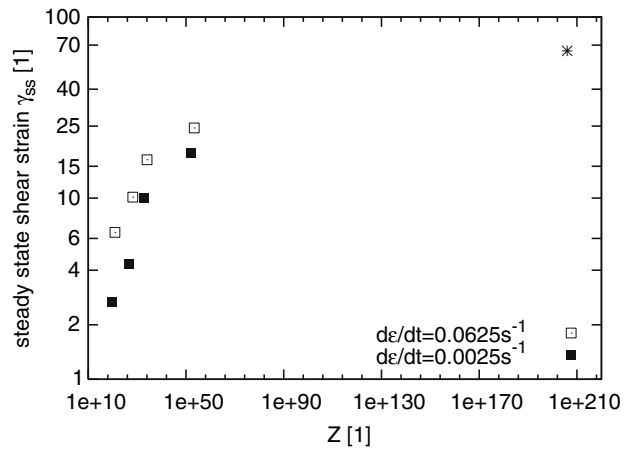

Fig. 15—Steady-state flow stress under the assumption of deformation of the material in the burr zone, as a function of Zener–Hollomon parameter in log (σ_{ss}) vs log (Z) scale. Note the data point at very large Z obtained from a sample deformed at 77 K.[23]

occurrence of a steady state rather than a DDRX; the latter seems to be impossible, due to the low grain-boundary mobility at these temperatures. This is supported by the fact that the observed behavior is similar to that reported for the pure iron[44] that was torsional deformed at warm-working conditions, corresponding to Zener–Hollomon parameters between 1×10^8 and 1×10^{18}. In this case, the occurrence of a steady state at large strains was also ascribed to geometrical DRX.

Increasing Z (*i.e.*, decreasing the temperature of deformation) reduces the thermally activated mobility of dislocations and, therefore, the rate of DRX. The larger remaining density of defects is stored in smaller microstructural elements (cells and cell blocks) (Figure 13), with boundaries of larger disorientations (Figure 10), which results in an increase in the steady-state flow stress (Figure 15). Because the geometrical DRX is characterized by a small-range migration of high-angle dislocation boundaries,[43] it is plausible that increasing Z leads to the observed increase in onset strain, as can be seen in Figure 16. The reduced thermally activated mobility of microstructural boundaries may inhibit the dynamical formation of equiaxed microstructural elements, which is observed during materials processing at warm-working conditions.[26,27,45–47] Therefore, the mean aspect ratio of the microstructural elements increases with increasing Z, as depicted in Figure 14.

B. High Z Regime

In the high Z regime, the flow curves again did not show any noticeable reduction when the strain exceeds the onset strain for the steady state. However, the fraction of low-angle boundaries (LABs) is now very small, and the slopes of the log (property) *vs* log (Z) curves are significantly smaller than in the low Z regime. Possible reasons for this significant change in the Z behavior of the steady-state properties are discussed here.

One reason for the occurrence of a high Z regime might be a significant change in the structural restoration process.

(a) In the low Z regime, the migration of microstructural boundaries (geometrical DRX) might be the dominating process in the steady state, in which dynamic recovery might play a minor role. The situation is possibly opposite in the high Z regime. At high Z, dynamic recovery may become more important, because with increasing Z, the volume fraction of highly disordered boundaries increases. These boundaries can act as sufficient sinks for glide dislocations, where the consumed dislocations may annihilate readily, due to the huge density of defects that are concentrated in these boundaries. This type of change in the structural restoration process would describe the shift of the onset strain of the steady state toward higher values, as one would estimate by simple extrapolation of the low Z regime because, due to the extended dynamic recovery, a higher amount of deformation would be necessary to initiate a process such as geometrical DRX. However, it would be difficult to describe the observed evolution of the microstructure solely by this change in the restoration mechanism. Another reason for the occurrence of a high Z regime might be a change in the dominant deformation mechanism.

(b) Below a certain size of the microstructural elements, it is possible that new glide dislocations are more frequently emitted from microstructural boundaries, because they become too small to activate dislocation sources in their interior. If these glide dislocations are then frequently consumed by opposite boundaries (as described earlier), the material is deformed without any significant change in the overall density of stored defects. Such a change in deformation micromechanism was proposed for SPD copper,[48] with microstructural elements between 600 and 200 nm in size. This type of change would again explain the observed shift in the onset of steady state toward larger shear strains, as can be seen in Figure 16. However, such a mechanism would lead to very elongated microstructural elements; these were not observed in the present study.

(c) The deformation mechanism may change from pure dislocation glide toward sliding along microstructural boundaries, when microstructural sizes fall below a certain critical size. Such behavior was proposed for pure copper,[48] for crystallites with sizes below 100 nm, and in aluminum and its alloys,[8,49] and was frequently discussed for submicron and nanocrystalline pure iron,[50,51] for microstructures with sizes of approximately 100 to 200 nm. This change in the micromechanism of plastic deformation would be a possible explanation for the lower steady-state flow stresses that are observed in the high Z regime, as one would expect by simple extrapolation of the low Z regime (Figure 15). Furthermore, this would be a reasonable explanation for the observed fact that microstructural elements bounded by HABs are less fragmented into subgrains, as is the case in the low Z regime (Figure 17), because when the deformation is governed for a significant fraction by sliding along microstructural boundaries, then the crystallites themselves are not plastically deformed, which may "protect" them from fragmentation. However, if sliding along microstructural boundaries becomes the dominant deformation mechanism, one would expect that the elongated microstructural elements are more aligned with the shear direction; this is an indicator that was not observed in the micrographs.

(d) It is also possible that the plastic deformation is realized by a collective, deformation-driven migration of LABs or HABs. The fact that, in the high Z regime, the microstructural elements with HABs are mainly subdivided by boundaries that are perpendicular to the direction of shear can be an indicator for such behavior.

Based on the results of this work, it is not easy to determine whether the change in a single mechanism is responsible for the occurrence of a high Z regime or several changes in the underlying micromechanism have to be taken into account simultaneously.

The Derby law is a very helpful tool for analyzing the steady-state deformation in the high-temperature regime.[52] The steady-state stress for different temperatures and strain rates, σ_{ss}, is plotted as a function of the resulting size of the grains or subgrains. The σ_{ss} is usually inversely proportional to the grain size to the power of p, where p is usually called the Derby parameter; it is between 0.5 and 1. It is assumed that the value depends on the proportion of grain boundaries and subgrain boundaries. It should be 0.5 and 1, in the case of grain boundaries and subgrain boundaries, respectively. The p is approximately 2/3, in the case of DRX. Plotting the values of Table III gives a p between 0.6 and 0.7. This again indicates for both the low Z and the high Z regime, the similarity of the SPD deformation and the restoration mechanism in the saturation region, with the phenomena taking place during DRX in hot working.

V. CONCLUSIONS

Armco Iron was severely deformed by means of HPT at a constant hydrostatic pressure of 5.4 GPa in the temperature range between 0.08 and 0.40 T_m. The flow stress was measured for the first time *in situ* during SPD and the resulting microstructure was investigated.

1. For all investigated deformation conditions (temperatures and strain rates), a saturation of both the size of the microstructural features (size of grains, texture, *etc.*) and the flow stress is obtained at large strains. Since the measured flow curves remain flat and no reduction was observed when the strain exceeds the onset strain of saturation, it is reasonable to term this state a steady state.
2. The decrease in deformation temperature or increase in strain rate results in an increase of both onset strain for saturation and appropriated saturation flow stress, for the whole range of investigated deformation parameters. Smaller crystallites (cell blocks obtained by EBSD and cells taken from BSE micrographs) were observed when deformation was performed at lower temperatures or higher strain rates. The microstructures exhibit solely elongated microstructural elements; their aspect ratio and mean angle of disorientation increase significantly with decreasing deformation temperature.
3. The observed steady-state properties can be sufficiently described by the Zener–Hollomon parameter; the range of investigated deformation parameters is divided into two regimes.
4. In a low Zener–Hollomon regime (a Z between 1×10^{22} and approximately 1×10^{35}), a CDRX process similar to geometric DRX seems to be responsible for the occurrence of the observed steady state at large strain.
5. A high Zener–Hollomon regime is observed at a Z larger than 1×10^{35}, where the slope of the ln (property) *vs* ln (Z) curves are significantly smaller than for the low Z regime; the microstructural sizes are significantly larger than is expected from the low Z regime; the resulting flow stress and the steady-state strain is smaller than one would expect by simple extrapolation of the low Z regime. Different mechanisms (change in restoration processes, change in deformation micromechanism toward dislocation movement from HAB to HAB, boundary sliding, or strain-induced boundary migration) are discussed. The transition from the low Z to the high Z regime could not be ascribed solely to one of these mechanisms; it might be a combination of them. Hence, further investigations are needed to understand better the deformation and structural restoration mechanism during SPD.

APPENDIX

Measurement of flow stress during HPT

For a conventional torsion test, the shear flow stress $\tau(\gamma)$ is generally integrated over the cross sections to equilibrate with the applied torque,[53–55] $\Gamma_t (\gamma)$:

$$\Gamma_t(\gamma) = 2\pi \int_0^a r^2 \tau(\gamma) dr \qquad [A1]$$

where a is the radius at the circumference of the sample. The extraction of the flow stress from Eq. [A1] can be made at the circumference of the sample.[53,56] If only the saturation is of further interest rather than the detailed hardening behavior of the material, as is the case in the present study, then the saturation shear flow stress τ_s is given as

$$\tau_s = \frac{3}{2\pi a^3} \Gamma_{t,s} \qquad [A2]$$

where $\Gamma_{t,s}$ is the measured saturation torque.

The torque measured *in situ* during HPT reflects the change of the flow stress of the processed materials at the given parameters shear strain γ, strain rate $\dot{\gamma}$, and deformation temperature T. Due to the geometry of the HPT tool used in the present study (Figure A1), the measured torque Γ consists of the torque Γ_d needed for the torsional deformation of the material in the cavity between the two anvils (deformation zone, $0 \leq r < r_i$) and a torque Γ_b that arises in the area of the burr (burr zone, $r_i \leq r < r_o$) that is formed during the loading of the tool before one of the anvils starts to rotate with respect
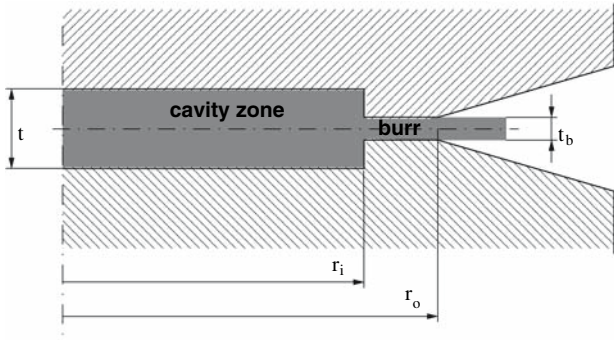
Fig. A1—Detailed sketch of the used tool with cavity zone and the area of the burr.[25]

to the other one. The saturation shear flow stress is then calculated by

$$\tau_s = \frac{3}{2\pi r_i^3} \Gamma_{d,s} \qquad [A3]$$

where $\Gamma_{d,s}$ represents the saturation torque arising in the deformation zone. This torque is calculated by subtracting the saturation torque arising in the burr zone $\Gamma_{b,s}$ from the totally measured torque Γ_s at saturation:

$$\Gamma_{d,s} = \Gamma_s - \Gamma_{b,s} \qquad [A4]$$

Depending on the behavior of the materials in the burr zone, the following two cases for the contribution of the burr to the totally measured torque can be distinguished.

A. Sliding between Burr and Tool

Assuming that slip between one side of the burr and the anvil is present, the torque arising in this area is given with

$$\Gamma_{b,\mu,s} = 2\pi\mu \int_{r_i}^{r_0} p(r) r^2 dr \qquad [A5]$$

where r_i and r_o are the radii of the inner and the outer edge of the burr, $p(r)$ describes the pressure in the burr zone as a function of the radius, r is the distance to the center of rotation, and μ represents the coefficient of friction. Recent results from finite element calculations[57] make it reasonable to assume for the given HPT tool a linear decrease from about 80 pct of the nominal hydrostatic pressure at the inner edge to the flow stress of the undeformed material at the outer edge of the burr. For this type of linear drop of pressure in the burr zone, the torque arising in this region is given by

$$\begin{aligned}
\Gamma_{b,\mu,s} &= 2\pi\mu \int_{r_i}^{r_0} \left(f_p \cdot p - r \cdot \frac{f_p \cdot p - 2\tau_0}{r_o - r_i} \right) r^2 dr \\
&= \mu \cdot \frac{\pi(r_o - r_i)}{6} \left[f_p \cdot p \left(3r_i^2 + 2r_i r_o + r_o^2 \right) \right. \\
&\quad \left. + 2\tau_0 \left(r_i^2 + 2r_i r_o + 3r_o^2 \right) \right] = \mu \cdot C
\end{aligned}$$

B. Deformation of the Materials That Form the Burr

In the case in which friction is sufficient to deform the material in the burr zone, the saturation torque arising in this area is given by

$$\Gamma_{b,d,s} = 2\pi \int_{r_i}^{r_0} r^2 \tau_{b,s} dr \qquad [A6]$$

where $\tau_{b,s}$ is the saturation flow stress in the burr zone. Due to the geometry of the tool, the strain rate in the burr zone is larger than in the deformation zone, which conventionally increases the flow stress in this area a little; this is expressed as $\tau_{b,d,s} \simeq (1 + \kappa)\tau_s$, where κ is a very small number, depending on the difference in strain rate between the deformation zone, the burr zone, and the processed material. The contribution of the burr zone to the total torque can then be expressed as a constant fraction, f_b, which is calculated as

$$f_b = \frac{r_o^3 - r_i^3}{r_i^3 \left(\frac{1}{1+\kappa} - 1 \right) + r_o^3} \qquad [A7]$$

The torque from the burr zone can then be expressed as

$$\Gamma_{b,d,s} = (1 - f_b) \cdot \Gamma_s \qquad [A8]$$

The effect in the variation of the friction coefficient of sliding, μ, and the steady-state stress increase due to the higher strain rate in the burr regions on the estimation of the steady-state flow stress is illustrated in Figure A2 by the fraction of the corrected steady-state flow stress, τ_s, and the uncorrected flow stress, $\tau_{s,\text{uncorrected}}$, determined from the measured torque. Assuming deformation of the material in the burr, the flow stress is only influenced by the parameter κ. In contrast, the flow stress determined under the assumptions of the sliding of the material in the burr against one of the anvils is much
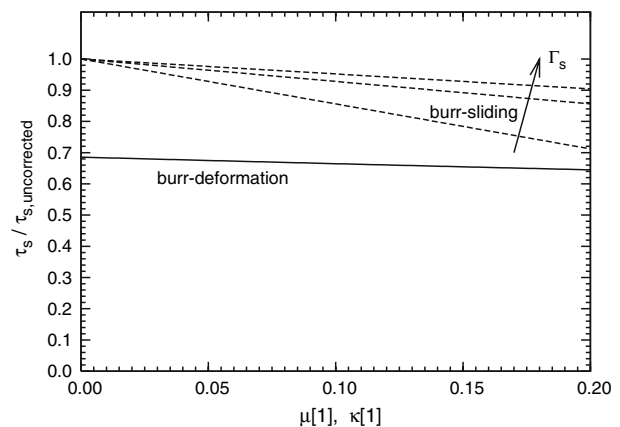

Fig. A2—Comparison of the fraction of corrected and uncorrected steady-state flow stress obtained from *in-situ* torque measurements during HPT, under the assumptions of sliding of the material that forms the burr against one anvil (dashed lines) and deformation of the burr material (solid line), respectively. See text for further description.[26]

more affected by the chosen coefficient of friction. In addition, $\tau_s/\tau_{s,\text{uncorrected}}$ depends on τ_s and, therefore, on Γ_s itself. An increase in Γ_s reduces the difference between τ_s and $\tau_{s,\text{uncorrected}}$.

REFERENCES

1. R.Z. Valiev, R.K. Islamgaliev, and I.V. Alexandrov: *Prog. Mater. Sci.*, 2000, vol. 45, pp. 103–84.
2. M.J. Zehetbauer, J. Kohout, and E. Schafler: *J. Alloys Compd.*, 2004, vol. 378, pp. 329–34.
3. M. Zehetbauer: *Acta Mater.*, 1993, vol. 41, pp. 589–99.
4. Y. Iwahashi, Z. Horita, and M. Nemoto: *Acta Mater.*, 1998, vol. 46 (9), pp. 3317–31.
5. B.Q. Han and S. Yue: *Mater. Process. Technol.*, 2003, vol. 136, pp. 100–04.
6. S.H. Lee, T. Sakai, and D.H. Shin: *Mater. Trans.*, 2003, vol. 44 (7), pp. 1382–85.
7. A. Vorhauer and R. Pippan: *Scripta Mater.*, 2004, vol. 51, pp. 921–25.
8. C. Xu, M. Furukawa, and Z. Horita: *Acta Mater.*, 2003, vol. 51, pp. 6139–49.
9. F.J. Humphreys, P.B. Prangnell, and J.R. Bowen: *Philos. Trans. R. Soc. London, Ser. A*, 1999, vol. 357, pp. 1663–81.
10. P.J. Apps, M. Berta, and P.B. Prangnell: *Acta Mater.*, 2005, vol. 53, pp. 499–511.
11. D.H. Shin, B.D. Ahn, and H.S. Cho: in *Ultrafine Grained Materials II*, D.H. Shin and T.C. Lowe, eds., Minerals, Metals and Materials Society, Warrendale, PA, 2004, pp. 421–26.
12. N. Tsuji, Y. Ito, and Y. Saito: *Scripta Mater.*, 2002, vol. 47, pp. 893–99.
13. D.H. Shin, J.J. Pak, and Y.K. Kim: *Mater. Sci. Eng.*, 2002, vol. 323, pp. 409–15.
14. A. Vorhauer, S. Kleber, and R. Pippan: *Mater. Sci. Eng., A*, 2005, vols. 410–411, pp. 281–84.
15. R.Z. Valiev: *Adv. Eng. Mater.*, 2003, vol. 5 (5), pp. 296–300.
16. T. Hebesberger, H.P. Stüwe, A. Vorhauer, and R. Pippan: *Acta Mater.*, 2005, vol. 53, pp. 393–402.
17. H.P. Stüwe: *Adv. Eng. Mater.*, 2003, vol. 5, pp. 291–300.
18. F. Wetscher: unpublished research, Hilti, Lichtenstein, 2005.
19. F. Wetscher and R. Pippan: *Philos. Mag.*, 2006, vol. 86, pp. 5867–83.
20. W.H. Huang, C.Y. Yu, and P.W. Kao: *Mater. Sci. Eng.*, 2004, vol. 366, pp. 221–28.
21. T. Sakai and J.J. Jonas: *Acta Metall.*, 1984, vol. 32, pp. 189–209.
22. S.J. Hales, T.R. McNelly, and H.J. McQueen: *Metall. Trans. A*, 1991, vol. 22A, pp. 1037–47.
23. K. Tsuzaki, X. Huang, and T. Maki: *Acta Mater.*, 1996, vol. 44, pp. 4491–99.
24. F.J. Humphreys and M. Hatherly: *Recrystallization and Related Annealing Phenomena*, Pergamon Press, Oxford, 1996, pp. 127–392.
25. S. Gourdet and F. Montheillet: *Mater. Sci. Eng., A*, 2000, vol. A283, pp. 274–88.
26. H.J. McQueen, E. Evangelista, and M.E. Kassner: *Z. Metallkd.*, 1991, vol. 82, pp. 336–45.
27. H.J. McQueen and E. Evangelista: *Czech. J. Phys., B*, 1988, vol. 38, pp. 359–72.
28. A. Belyakov, T. Sakai, and H. Miura: *ISIJ Int.*, 1999, vol. 39, pp. 592–99.
29. A. Belyakov, T. Sakai, and H. Miura: *Acta Mater.*, 2002, vol. 50, pp. 1547–57.
30. M.E. Kassner, H.J. McQueen, and E. Evangelista: *Mater. Sci. Forum*, 1993, vols. 113–115, pp. 151–56.
31. N. Tsuji, R. Ueji, and Y. Ito: *Proc. 21st Riso Int. Symp. on Materials Science*, Riso National Laboratory, Denmark, 200, pp. 105–14.
32. M.R. Druby and F.J. Humphreys: *Acta Metall.*, 1986, vol. 34, pp. 2259–71.
33. P. Cizek and B.P. Wynne: *Mater. Sci. Eng., A*, 1997, vol. 230, pp. 88–94.
34. A. Belyakov, R. Kaibyshev, and R. Zaripova: *Mater. Sci. Forum*, 1993, vols. 113–115, pp. 385–89.
35. C.G. Schmidt, C.M. Young, and B. Walser: *Metall. Trans. A*, 1982, vol. 13A, pp. 447–56.
36. H.J. McQueen, W.A. Wong, and J.J. Jonas: *Can. J. Phys.*, 1967, vol. 45, pp. 1225–39.
37. W.A. Wong and J.J. Jonas: *Trans. TMS-AIME*, 1968, vol. 242, pp. 2271–80.
38. H.J. McQueen and N. Ryum: *Scand. J. Metall.*, 1985, vol. 14, pp. 183–94.
39. H.J. McQueen and W. Blum: *Mater. Sci. Eng., A*, 2004, vol. 290, pp. 95–107.
40. J. Philibert: *Atom Movements—Diffusion and Mass Transport in Solids, Number 110*, Les Editions de Physique, Les Ulis, France, 1991, pp. 74–81.
41. D.W. James and G.M. Leak: *Philos. Mag.*, 1966, vol. 14, pp. 701–13.
42. H.J. Frost and M.F. Ashby: *Deformation-Mechanism Maps—The Plasticity and Creep of Metals and Ceramics*, Pergamon Press, Oxford, 1982, pp. 60–74.
43. H.J. McQueen, J.K. Solberg, and N. Ryum: *Philos. Mag. A*, 1989, vol. 60, pp. 447–71.
44. G. Glover and C.M. Sellars: *Metall. Trans.*, 1973, vol. 4, pp. 765–75.
45. F. Schuh and M. von Heimendahl: *Z. Metallkd.*, 1974, vol. 65, pp. 346–52.
46. A. Korbel, M. Richer, and J. Richert: *Deformation in Polycrystals: Mechanism and Microstructures*, Riso National Laboratory, Roskilde, Denmark, 1981, pp. 445–50.
47. H. Hero and C.J. Simenson: *Scand. J. Metall.*, 1972, vol. 1, pp. 115–20.
48. E.V. Kozlov, A.N. Zhdanov, and N.A. Popova: *Mater. Sci. Eng., A*, 2004, vols. A387–A389, pp. 789–94.
49. Y. Huang and T.G. Langdon: *Mater. Sci. Eng., A*, 2003, vol. 358, pp. 114–21.
50. R.Z. Valiev, Y.V. Ivanishenko, and E.F. Rauch: *Acta Mater.*, 1996, vol. 44, pp. 4705–12.
51. S. Takaki, K. Kawasaki, and Y. Kimura: *Mater. Process. Technol.*, 2001, vol. 117, pp. 359–63.
52. B. Derby: *Acta Metall. Mater.*, 1991, pp. 955–62.
53. H.P. Stüwe and H. Turk: *Z. Metallkd.*, 1964, vol. 55, pp. 699–703.
54. M. Zhou and M.P. Clode: *Mech. Mater.*, 1998, vol. 27, pp. 63–76.
55. F. Wetscher, A. Vorhauer, and R. Pippan: *Mater. Sci. Eng., A*, 2005, vols. 410–411, pp. 213–16.
56. D.S. Fields and A.W. Backofen: in *Proc. ASTM*, 1957, vol. 57, pp. 1259–72.
57. W. Ecker: Master's thesis, University of Leoben, Austria, 2004.